processes

MDPI

Article

Zeolites Derived from Natural Kaolinite for CO_2 Adsorption

Giorgio Celoria [1], Federico Begni [1], Geo Paul [1], Enrico Boccaleri [2,3,*], Valentino Merlo [4], Leonardo Marchese [1] and Chiara Bisio [1,5,*]

[1] Dipartimento di Scienze e Innovazione Tecnologica, Università del Piemonte Orientale A. Avogadro, Viale T. Michel 11, 15121 Alessandria, Italy; giorgio.celoria@uniupo.it (G.C.); federico.begni@uniupo.it (F.B.); geo.paul@uniupo.it (G.P.); leonardo.marchese@uniupo.it (L.M.)
[2] Dipartimento per lo Sviluppo Sostenibile e la Transizione Ecologica, Università del Piemonte Orientale A. Avogadro, Piazza S. Eusebio 5, 13100 Vercelli, Italy
[3] UPO4Sustainability Center, Viale T. Michel 11, 15121 Alessandria, Italy
[4] Built—Buzzi Innovation Lab and Technology, Via Restano 3, 13100 Vercelli, Italy; valentino.merlo@buzzi.com
[5] CNR-SCITEC Istituto di Scienze e Tecnologie Chimiche "Giulio Natta", Via G. Venezian 21, 20133 Milano, Italy
* Correspondence: enrico.boccaleri@uniupo.it (E.B.); chiara.bisio@uniupo.it (C.B.); Tel.: +39-0131-360264 (E.B.); +39-0131-360216 (C.B.)

Abstract: This manuscript deals with the synthesis of different types of zeolites from natural kaolinite samples for CO_2 adsorption. A zeolite A was prepared from kaolinite by means of an alkaline fusion process, followed by hydrothermal treatment, whereas a highly crystalline zeolite X was synthesized by optimizing the previously mentioned synthetic procedure. In detail, the SiO_2/Al_2O_3 molar ratio in the preliminary mixture was modified with the addition of a secondary silicon source (sodium silicate) in order to obtain the one required for zeolites X. The physicochemical properties of the pristine clay and of the different zeolites were investigated by means of a multi-technique approach, including XRPD; SEM-EDX; ^{23}Na, ^{27}Al and ^{29}Si MAS NMR spectroscopy; and N_2 physisorption analysis at 77 K. Since the Si and Al molar ratios and reactivities are key parameters for the synthesis of zeolites, these aspects, primarily related to the use of a naturally occurring aluminosilicate as the raw material, have been investigated for their correlation with the physicochemical properties of the synthetic products. Moreover, by means of a custom-built volumetric apparatus, the CO_2 adsorption capacity of the resulting zeolites at low gas pressures (<1 bar) and at 25 °C was assessed.

Keywords: zeolite LTA; zeolite X; natural kaolinite; alkaline fusion; Si/Al ratio; CO_2 adsorption

Citation: Celoria, G.; Begni, F.; Paul, G.; Boccaleri, E.; Merlo, V.; Marchese, L.; Bisio, C. Zeolites Derived from Natural Kaolinite for CO_2 Adsorption. *Processes* **2024**, *12*, 194. https://doi.org/10.3390/pr12010194

Academic Editor: Antoni Sanchez

Received: 30 December 2023
Revised: 12 January 2024
Accepted: 14 January 2024
Published: 16 January 2024

1. Introduction

In the last decades, the continuous spreading of greenhouse gases (i.e., CO_2 and CH_4) in the atmosphere from anthropogenic activities has raised global concerns regarding their effects on the Earth's climate [1,2]. Due to enhancing greenhouse effects on the atmosphere, the rise in the concentration of CO_2, by the increased emissions since the beginning of the 20th century, has caused an increase in global temperatures [3]. The global climate impact has led to a series of current and forthcoming adverse effects on the ecosystem, such as a rise in the sea level from melting ice, life-threatening weather events and uncontrolled climate changes [3]. Amongst the coping strategies to reduce the anthropogenic impacts on the global ecosystems to prevent irremediable compromises, researchers are even more focused on the development of efficient and cost-effective methods to reduce the amount of released CO_2 [4,5]. In addition to preventing emissions by switching energy sources to renewable technologies, capture, storage and utilization of carbon dioxide (CCS/CCU) are considered key processes for the perspective of the net-zero emission scenario to be pursued by 2050 [6,7]. Within this scope, membranes [8], liquid amine-based technologies [9] and calcium looping [10] are now considered attractive technologies for the separation and storage of CO_2 in post-combustion conditions. It has to be taken into account that amine-based methods suffer from corrosion issues and the chemicals and regeneration processes

are known to be expensive [9], whereas for calcium looping the thermal regeneration of the Ca-based sorbents, which is performed at approximately 1000–1200 °C, is energetically demanding [10].

Among the methods for the capture of CO_2, adsorption consists of a cost-effective, selective and efficient process that involves the use of a solid material that employs non-covalent interactions between the surface of the adsorbent and the adsorbate molecules [11,12]. The key aspect of adsorption is the choice of the host material that should have a high specific surface area and high pore volume but also the capacity to interact with the guest molecules by means of specific surface features, such as the ions of functional groups [13].

Thanks to the well-defined microporous structure [14], high specific surface area and pore volume [14,15], zeolites are widely employed as molecular sieves for the adsorption of small molecules, such as CO_2 [16]. Zeolites are a wide category of microporous crystalline aluminosilicates based on a three-dimensional framework of interconnected silicon and aluminum tetrahedral oxide units [14,17,18]. The isomorphic substitution of Si^{IV} with Al^{III} atoms introduces in the framework a negative charge located on the bridging oxygen atom between the Si and Al atoms. These negative charges are balanced by extra-framework cations (i.e., Na^+, Li^+, K^+ and Ca^{2+}) or protons that are usually present within the cavities of the material [14,19].

Zeolites are both natural minerals and produced by synthetic procedures. For the synthesis of these materials, the control of composition and features is now leading the industrial production of zeolites [20,21]. Zeolites are classified according to the IZA (International Zeolite Association) coding [22].

By considering the growing need for efficient and cost-effective CO_2 adsorbents, the work presented here deals with the synthesis of a zeolite A and a zeolite X from a natural aluminosilicate (kaolinite). These samples were both tested as solid adsorbents for the adsorption of CO_2 at low gas pressures ($\leq$1 bar) and 25 °C. Kaolinite is a largely available natural clay, featuring a layered structure based on a silicate tetrahedral layer and an aluminium-based octahedral layer according to the so-called TO (or 1:1) structure [11,23–25]. Its mineralogical composition is $Al_2Si_2O_5(OH)_4$. The mineral is a commodity for the industry of ceramics [26] and, in this work, it is employed as a cheap and widely available Si and Al source for the preparation of zeolite samples. By following the main steps reported in the literature [27–29], a zeolite A was prepared through the alkaline fusion of natural kaolinite, followed by hydrothermal treatment. Briefly, alkaline fusion involves the mineralization at high temperatures in the solid state with a Si- and Al-rich precursor in the presence of an alkali activator (i.e., NaOH) to form a mixture of silicate and aluminate salts [21,30,31]. Next, the obtained mixture is usually stirred with water and hydrothermally treated to promote gel crystallization [18].

In order to prepare high-purity zeolite X with a different SiO_2/Al_2O_3 molar ratios with respect to kaolinite, the alkaline fusion process was optimized upon the addition of a secondary silicon source (sodium silicate) within the preliminary mixture. We focused our interest on zeolites X because they are considered one of the most performant adsorbent materials for CO_2 adsorption [14,16]. In fact, these types of adsorbents have proven to be particularly suitable for CO_2 adsorption applications retaining up to 3 $mmol \cdot g^{-1}$ at 1 bar and 25 °C [16,32].

As reported in the literature, each zeolite requires a specific SiO_2/Al_2O_3 molar content to be prepared [29,33]. For zeolites A and zeolites X the SiO_2/Al_2O_3 ratio of 2 and 3.2, respectively, is needed [29,33]. Indeed, the SiO_2/Al_2O_3 molar ratio is a crucial parameter that has to be considered during the synthesis of zeolites [29,33]; this aspect is usually not explored in the context of the alkaline fusion processes of natural clays.

In light of these considerations, the aim of this work is to modify the Si and Al molar content in the preparation mixture to prepare a specific zeolite using the alkaline fusion process with a natural aluminosilicate. Moreover, by considering that the physicochemical properties (i.e., structural, morphological and textural properties) of zeolites prepared through the alkaline fusion of natural kaolinite have been only partially explored in the

literature, in this manuscript, we provide a more detailed description about this topic. Thus, we have adopted a multi-technique approach, that includes XRPD; Rietveld semi-quantitative analysis; ^{23}Na, ^{27}Al and ^{29}Si MAS NMR spectroscopy; SEM-EDX; and N_2 physisorption analysis at 77 K, to fully characterize the obtained materials.

Moreover, the excess adsorption of CO_2 in zeolite A and zeolite X was assessed at 25 °C and at low gas pressures (i.e., $\leq$1 bar) by means of a stainless steel custom-built volumetric apparatus. In addition, the lifetime and stability of zeolite X prepared from kaolinite were investigated over two CO_2 adsorption/desorption cycles. This aspect is not usually investigated within studies regarding the synthesis of zeolites from natural clay, but it can become of crucial importance to assess the lifetime and stability of an adsorbent material [11].

2. Materials and Methods

2.1. Materials

The chemicals that were used are natural kaolinite ($Si_2Al_2O_7{\cdot}2H_2O$, CAS: 1318-74-7, M.W. 258.16 g·mol^{-1}, SigmaAldrich®, Darmstadt, Germany), anhydrous sodium metasilicate (Na_2SiO_3, CAS: 6834-92-0, M.W. 122.06 g·mol^{-1}, Alfa Aesar®, Haverhill, MA, USA) and sodium hydroxide (NaOH, CAS: 1310-73-2, M.W. 39.99 g·mol^{-1}, Merck KGsA, Darmstadt, Germany).

2.2. Methods

2.2.1. Zeolite A Synthesis

Following the main experimental steps described in the literature [28,34], 2 g of natural kaolinite was ground with 4 g of NaOH to form the preliminary mixture, which was transferred inside a ceramic crucible and treated at 200 °C for 4 h in a muffle furnace. Subsequently, the solid was ground again in a ceramic mortar, and it was stirred inside a 100 mL round-bottom flask with 40 mL of deionized water for 2 h at 50 °C in a thermostatic water bath. Finally, the gel was transferred inside a steel autoclave equipped with a 100 mL PTFE vessel, and it was treated at 90 °C for 17 h inside an electric furnace. Next, the solid was recovered through Büchner filtration and washed with deionized water until a neutral pH, and then the powder was dried at 100 °C overnight. At the end of the process, 2.1 g of zeolite A (hereafter named ZEO A) was obtained.

2.2.2. Zeolite X Synthesis

A pure zeolite X was obtained upon the optimization of the alkaline fusion process described in Section 2.2.1. According to the literature, to prepare a zeolite X, a SiO_2/Al_2O_3 molar ratio of 3.2 is required [29,33]. In this respect, by considering that the chemical formula of the parent kaolinite is $Si_2Al_2O_7{\cdot}2H_2O$, to obtain the suitable Si and Al content, 0.97 g of Na_2SiO_3 was ground in a ceramic mortar with 2 g of kaolinite and 4 g of NaOH. Next, the mixture was treated at 200 °C for 4 h in a muffle furnace. Then, the solid was ground again, and the fine powder was stirred with 46 mL of deionized water in a 100 mL round-bottom flask at 50 °C for 2 h. The temperature was kept at 50 °C by means of a thermostatic water bath. Finally, the suspension was transferred inside a steel autoclave equipped with a 100 mL PTFE vessel, and the hydrothermal treatment of the gel was performed at 90 °C for 17 h. Subsequently, the solid was recovered through Büchner filtration and copiously washed with deionized water until a neutral pH was reached. After being dried at 100 °C overnight, 2 g of powder was obtained. This material was named ZEO X.

2.2.3. XRPD Analysis

The X-ray powder diffraction (XRPD) patterns of the samples were collected with a Bruker D8 Advance diffractometer (Karlsruhe, Germany) with Bregg–Brentano Geometry using a Cu anode X-ray source (λ = 1.5418 Å) equipped with a Ni filter and operating at 40 kV and 40 mA. The patterns were collected in a 2θ range of 5–50° 2θ, with 2θ steps

of 0.02 and an acquisition time of 0.2 s/step. The anti-scatter knife was automatically synchronized, and the illumination area of the sample was kept constant at 17 mm^2 all across the measurements. Semi-quantitative mineralogical analyses were conducted by the Rietveld method using the Topas 6.0 package (software was commercially supplied by Bruker AXS, Karlsruhe, Germany). The refinements were conducted in the whole 5–50° 2θ range by using a 5th-order Chebychev polynomial for the background calculation and allowing for refinement of the sample displacement; the crystal size of all structures was set freely to vary between 32 and 1000 nm.

2.2.4. SEM-EDX

The SEM micrographs of the different materials were obtained by means of a scanning electron microscope (SEM) JEOL JSM-5600 LV (Milan, Italy) operating at 15 KV with an EDS detector attachment. Before SEM analyses, the surfaces of the sample were sputtered with a 20 nm layer of platinum. For each sample, EDS measurements were performed three times in different areas, and the average results were calculated.

2.2.5. MAS-NMR Measurements

^{29}Si, ^{27}Al and ^{23}Na NMR measurements were performed with a wide bore 11.75 Tesla magnet on a Bruker Avance III 500 spectrometer with operational frequencies of 99.35, 130.33 and 132.29 MHz, respectively. A sample spinning rate (magic angle spinning) of 10–15 kHz was used with a 4 mm triple resonance probe. All the ^{29}Si MAS NMR spectra were recorded under high-power proton decoupling conditions while the ^{27}Al MAS spectra were acquired with a large sweep width and small pulse angle ($\pi/12$) to ensure quantitative interpretation. Similarly, the ^{23}Na MAS spectra were acquired with a $\pi/12$ pulse in the absence of ^{1}H decoupling. For the ^{29}Si, ^{27}Al and ^{23}Na NMR, relaxation delays of 60, 1 and 1 s, were used, respectively. Chemical shift referencing was performed using external standards, such as the $Al(H_2O)_6{}^{3+}$ ion in 1.0 M $AlCl_3$ solution set to 0.0 ppm and TMS set to 0.0 ppm.

2.2.6. N_2 Physisorption Analysis at 77 K

The N2 physisorption analyses were performed on an Autosorb 6100 (Anton Paar S.r.L., Rivoli, Italy) at 77 K in the pressure range between 1×10^{-7} and 1 P/P_0 of relative pressure. Prior to the measurements, the samples were treated at 170 °C for 16 h. The specific surface area of the samples was determined by the Brunauer–Emmett–Teller (BET) multipoint method and the optimal linear range was selected by using a micropore BET assistant (IUPAC/Rouquerol method) from Kaomi 1.00 [Build:3] with Autosorb software (the obtained R^2 was 0.9998). The pore size distributions were obtained through the DFT method (silica/zeolite, adsorption branch model, cylindrical pores).

2.2.7. CO_2 Adsorption Measurements

A custom-built manual volumetric apparatus was employed to assess the CO_2 adsorption capacity at 25 °C and up to 1 bar of gas pressure for the different materials. The snapshot and the building scheme of the volumetric apparatus are shown in Figure S1. For more details about the experimental steps to determine the excess of CO_2 adsorbed see the Supporting Information.

3. Results

The structural properties of kaolinite, ZEO A and ZEO X were investigated by means of XRPD analysis. The XRPD patterns of the different materials are shown in Figure 1. XRPD patterns are indexed to identify the mineral phases present.

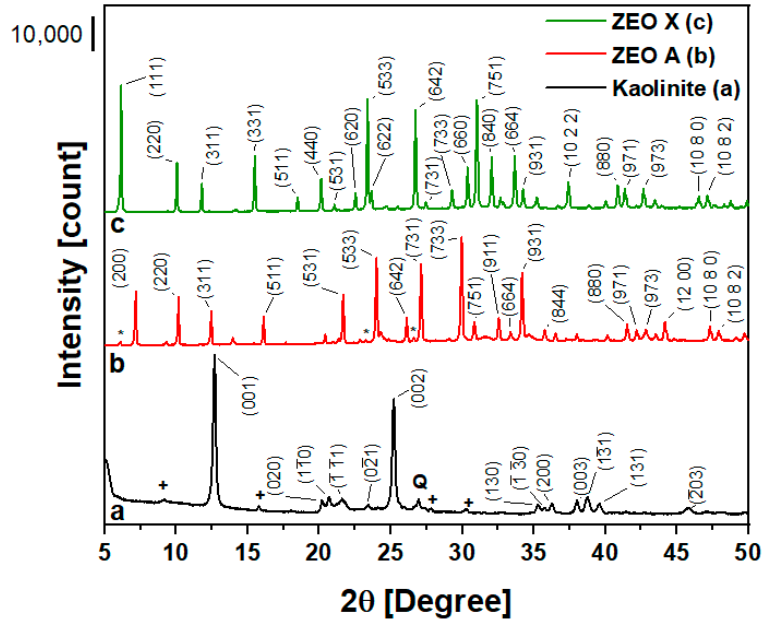

Figure 1. XRPD patterns of kaolinite (a), ZEO A (b) and ZEO X (c). Illite, chabazite and montmorillonite impurities within the parent kaolinite are marked with + symbols, whereas the zeolite X impurities within ZEO A are highlighted with * symbols.

The XRPD pattern of the parent clay (Figure 1a) is mainly dominated by the reflections of kaolinite, thus giving an indication that the starting product has a high purity grade. In detail, the most intense reflections at about 12° and 25° 2θ are related to the (001) and (002) planes, whereas those between 20°–25° and 35°–40° 2θ are assigned to the (020), (110), (111), (0 21), (130), (130), (200), (003), (131), (131), (201), and (203) planes of kaolinite, respectively [11,35].

Moreover, the sample contains traces of quartz, whose reflection is at 27° 2θ (labelled with Q in Figure 1), and illite, chabazite and montmorillonite (marked with+) that are usually present as impurities within natural clays [36–38]. However, as can be derived from the results of the Rietveld semiquantitative analysis (Table S1), kaolinite is the most abundant phase (84 wt.%), whereas the other impurities represent only 16 wt.%.

The alkaline fusion process producing the sample ZEO A has led to a substantial change in the structural properties of kaolinite. As it can be derived from the results of the XRPD analysis (Figure 1b), the diffraction pattern of the product mainly contains the typical reflections of zeolite A [39,40] that were assigned by means of the DIFFRAC.EVA V2 software and PDF2 database (2004) to their corresponding Miller indexes. As it can be derived from the results of the Rietveld semiquantitative analysis (see Table S2), this phase corresponds to 80.1 wt.%, thus suggesting that the kaolinite was almost completely converted into a zeolite A. In addition, three exceedingly weak reflections at 6°, 23.2° and 26.6° 2θ (marked with asterisks) suggest that only tiny traces of a zeolite X are present, i.e., the 1.1 wt.% (see Table S2) [16,40]. A possible explanation of these results could be related to the presence of Si-rich impurities, such as quartz (SiO_2), illite $(Si_4)(Al)_{2.3}O_{10}(OH)_2(H_2O)$ [41] and montmorillonite $Na_{0.33}(Al_{1.67}Mg_{0.33})Si_2O_{10}(OH)_2(H_2O)$ [41] (see Figure 1a, Tables 1 and S1), in the parent kaolinite. Since zeolites X require a higher Si content than zeolites A [29,33], it is probable that a small fraction of zeolite X could have formed. This hypothesis is corroborated by the fact that the reflections of quartz, illite and montmorillonite are not present in detectable amounts in the XRPD pattern of ZEO A (Figure 1b), thus indicating that these phases were solubilized along with kaolinite during the alkaline fusion process.

Table 1. EDX analysis of kaolinite, ZEO A and ZEO X. The average of three measurements are reported.

	Kaolinite		ZEO A		ZEO X	
Element	**At.%**	**Dev.st**	**At.%**	**Dev.st**	**At.%**	**Dev.st**
Si	19.36	0.54	19.85	0.39	16.60	0.22
Al	16.46	0.80	16.59	0.33	13.18	0.18
O	63.41	1.59	51.06	0.76	58.29	0.49
Na	0.21	0.16	12.50	0.31	11.93	0.19
K	0.57	0.07	/	/	/	/

On the other hand, the XRPD pattern of ZEO X (Figure 1c) is dominated by the reflections of a zeolite X, as assigned by means of the DIFFRAC.EVA software and PDF2 database (2004) to their corresponding Miller indexes. No other reflections were observed, thus indicating that the impurities within the parent clay were mineralized along with kaolinite during alkaline fusion (see Table S2). The results of the analysis reveal that the addition of sodium silicate to increase the SiO_2/Al_2O_3 ratio in the preliminary mixture from ca. 2 to 3.2 [29,33] is helpful to obtain a pure zeolite X.

To integrate the results of the XRPD analyses, the ^{27}Al and ^{29}Si MAS NMR measurements, which can reveal both crystalline and amorphous phases [42], were carried out (Figure 2). The ^{27}Al MAS NMR spectrum of the parent kaolinite (Figure 2, left panel) is dominated by an intense signal at 3 ppm related to the Al nuclei in an octahedral coordination located within the octahedral layers of kaolinite and of montmorillonite impurities [27,38,43]. Moreover, in the tetrahedral region (i.e., between 50 and 70 ppm), two low-intensity bands (marked with asterisks) due to the Al nuclei in tetrahedral configuration within the tetrahedral layers of illite and montmorillonite impurities are visible [11,38]. The ^{29}Si MAS NMR spectrum of kaolinite (Figure 2, right panel) is characterized by the presence of two sharp peaks at −91 and −92 ppm attributed to the Si nuclei in a tetrahedral configuration within the T-layers of kaolinite with three Si-O-Si bonds and one Si-O-Al bond formed through a non-bridging oxygen atom [$Si(OSi)_3(OAl)$] [42,44].

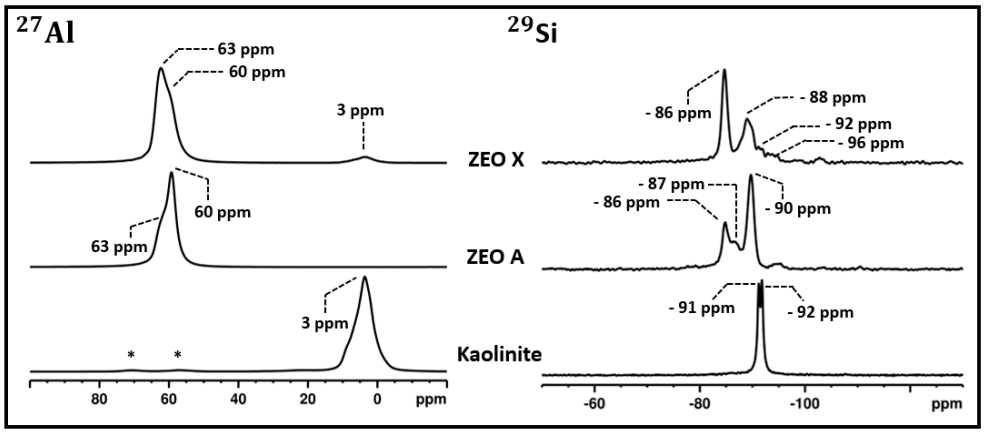

Figure 2. ^{27}Al (**left** panel) and ^{29}Si MAS NMR spectra (**right** panel) of kaolinite, ZEO A and ZEO X. The signals related to the ^{27}Al nuclei in tetrahedral coordination within the illite and montmorillonite impurities in the parent kaolinite are marked with '*'.

The ^{27}Al MAS NMR spectrum of ZEO A (Figure 2, left panel) shows the complete disappearance of the signal at 3 ppm due to the hexacoordinated Al nuclei, whereas a new peak at 60 ppm related to the Al nuclei in a tetrahedral coordination, typical of a zeolite A sample, appeared [45–47]. The shoulder at 63 ppm might be related to the presence of different tetrahedral Al species within ZEO A that might result from the slow dissolution of the parent kaolinite in alkali conditions [48].

The ^{29}Si MAS NMR spectrum of ZEO A (Figure 2, right panel) is characterized by several signals. The most intense peak at −90 ppm corresponds to the Q^4(4Al) Si nuclei in tetrahedral coordination, as expected for a zeolite A, that is characterized by four Si-O-Al bonds (i.e., $[Si(OAl)_4]$) [45,46]. In our case, the other signals at −86 and −87 ppm are probably ascribed to other $[SiO_4]^{4-}$ species formed during the alkali dissolution of natural kaolinite and which might have participated in zeolite germ formation [48].

The ^{27}Al MAS NMR spectrum of ZEO X (Figure 2, left panel) contains two signals at 3 and 63 ppm. The band at 63 ppm is assigned to the ^{27}Al nuclei in a tetrahedral coordination within the framework of zeolite X [49,50], whereas the shoulder at ca. 60 ppm might arise from different tetrahedral Al species within the sample derived from the slow dissolution of the parent kaolinite in alkali condition [48]. The presence of a low-intensity peak at 3 ppm suggests that the sample contains traces of residual hexacoordinated Al nuclei from the parent clay that were not mineralized during alkaline fusion. Crystalline phases related to possible species, consistent with this evidence, are not observed in the XRPD pattern of ZEO X (Figure 1c), probably because of their amorphous composition. The ^{29}Si MAS NMR spectrum of ZEO X shown in Figure 2 (right panel) is characterized by different signals related to Si nuclei in tetrahedral coordination within the framework of the sample [51]. The most intense peak at −86 ppm is due to the Q^4(4Al) Si nuclei [51] ($[Si(OAl)_4]$, as well as the band at −88 ppm is assigned to the Q^4(3Al) Si nuclei [51] ($[Si(OAl)_3(OSi)]$. At lower ppm, the band at −92 ppm is related to the Q^4(2Al) species, hence the Si nuclei with two Si-O-Si bonds and two Si-O-Al bonds (i.e., $[Si(OAl)_2(OSi)_2]$, whereas the signal at −96 ppm indicates the presence of Q^4(1Al) Si nuclei that are characterized by one Si-O-Al bond and three Si-O-Si bonds, $[Si(OSi)_3(OAl)]$ [51].

By considering that NaOH was employed as a mineralizing agent for the synthesis of ZEO A and ZEO X, it is probable that both of the zeolites are in the Na^+ form, hence with Na^+ extra-framework cations that counterbalance the negative charges that arise from the presence of the Al^{III} atoms [14]. In this respect, ^{23}Na MAS NMR spectroscopy provides an efficient tool to investigate this aspect. The ^{23}Na MAS NMR spectra of kaolinite, ZEO A and ZEO X are shown in Figure 3.

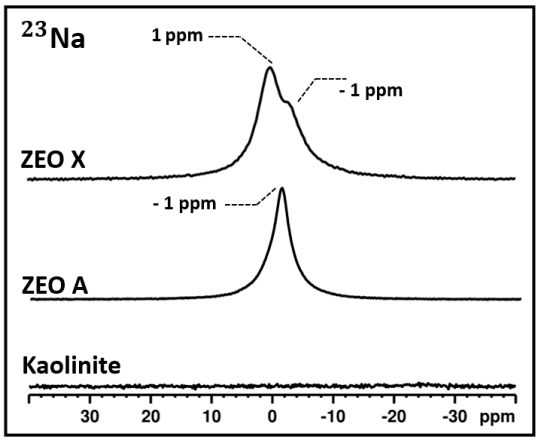

Figure 3. ^{23}Na MAS NMR of kaolinite, ZEO A and ZEO X.

In the ^{23}Na MAS NMR spectrum of the pristine kaolinite (Figure 3), no signals from ^{23}Na nuclei were observed, as natural kaolinites are usually characterized by a reduced isomorphic substitution ratio between the Si^{IV} and Al^{III} atoms within the T-layers, hence the extra-framework cations that could be located in the inter-layer spaces are nearly completely absent [23,34,52].

The ^{23}Na MAS NMR spectrum of ZEO A is characterized by a sharp peak at −1 ppm that is due to the Na nuclei balancing the zeolite A negative framework [53]. As reported in the literature, the extra-framework cations could populate three distinct lattice positions within a zeolite A (see below Figure S2A): the center of the six-rings on the threefold axis

(inside the sodalite cage, Site I), in the eight-ring supercage of zeolite A (Site II) and in the four-ring site, near the entrance of the supercage (Site III) [40,54].

The ^{23}Na MAS NMR spectrum of ZEO X (Figure 3) shows the presence of two broad signals at 1 and −1 ppm, which are both assigned to different species of Na^+ extra-frameworks cations that populate different lattice positions [53]. In the case of zeolites X, a cation could be located in the sodalitic cages (site I/I′), in the hexagonal rings inside the cavities (site II/II′) and in the entrances to the supercages (site III/III′) [14] (see below Figure S2B).

The morphological properties of kaolinite, ZEO A and ZEO X samples were investigated by means of SEM microscopy. Typical micrographs of kaolinite (a), ZEO A (b) and ZEO (X) are shown in Figure 4.

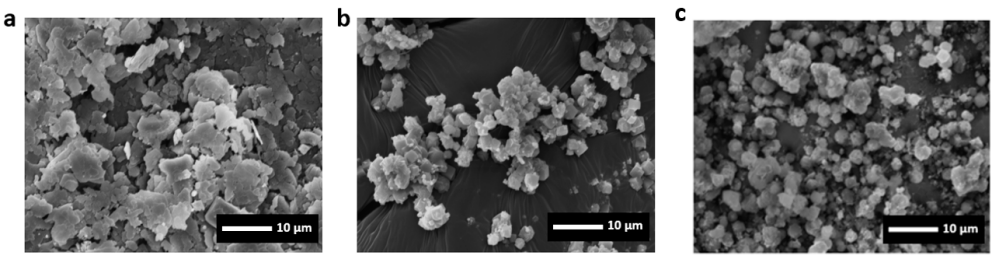

Figure 4. SEM micrographs at a magnification of 2000× of kaolinite (**a**), ZEO A (**b**) and ZEO X (**c**).

The SEM micrograph of the parent clay (Figure 4a) reveals that kaolinite has a layered morphology, with clusters of lamellae of variable dimensions from 5 to 15 µm. After the alkaline fusion process and hydrothermal treatment, the particles composing ZEO A and ZEO X samples appear quite different from that of the parent sample. In fact, ZEO A is characterized by well-defined cubic-shaped crystallites of about 0.5–1 µm, whereas ZEO X is made up of cubic/octahedral crystallites of ca. 0.5–1 µm. Similar results were observed in the literature [28,55].

The chemical composition of the different materials was determined through EDX analysis (Table 1). The chemical composition of the parent kaolinite (Table 1) is typical of an aluminosilicate material. The at.% of Si is slightly higher than that of Al, as the parent clay contains quartz, illite and montmorillonite impurities

Na and K are present as extra-framework cations to counterbalance the negative charges arising from the isomorphic substitution between Si and Al atoms in the T-layers of kaolinite and montmorillonite impurities [56]. However, their at.% is low, as montmorillonite impurities are present in a small amount (see Table S1) and the T-layers of natural kaolinites are usually characterized by a low isomorphic substitution ratio [23,34,52]. For this reason, no signals related to the ^{23}Na nuclei were observed in the ^{23}Na MAS NMR spectrum of kaolinite (Figure 3).

The at.% of Si and Al within ZEO A is quite similar to that of the parent clay (Table 1), as no additional Si and/or Al sources were added to the preliminary mixture. As was previously described, Na^+ cations are now present as extra-framework cations to counterbalance the negative charges due to the presence of Al atoms [14].

On the other hand, ZEO X is characterized by Si and Al at.% of 16.60% and 13.18%, respectively (see Table 1), with the Si/Al molar ratio of 1.26. These results are in agreement with the literature and due to the fact that sodium silicate was added. To give an example, in Z. Tahraoui's work [40], it is reported that a Na-X zeolite has a Si/Al molar ratio of 1.23. The difference in the ZEO X sample is consistent with the signals of octahedral Al moieties in ^{27}Al MAS NMR (Figure 2, left panel), showing that a part of the starting kaolinite, probably in amorphous form, which is commonly found after thermal treatments, was not converted during the optimized alkaline fusion. The presence of Na comes from the use of NaOH for the alkali fusion process [14].

The textural properties of the parent kaolinite, ZEO A and ZEO X were investigated by means of N_2 physisorption analysis at 77 K. The N_2 adsorption–desorption isotherms of the

samples and the DFT pore size distribution of ZEO X (silica/zeolite, ads. branch method, cylindrical pores) are shown in Figure 5. In Table 2 the SSA_{BET} and the pore volumes of the different materials are reported.

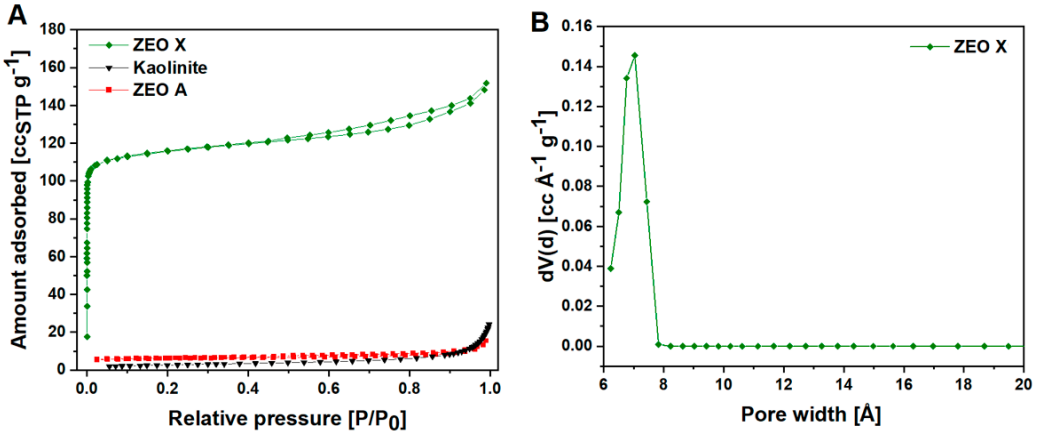

Figure 5. N_2 adsorption-desorption isotherms of kaolinite (triangles), ZEO A (squares) and ZEO X (rhombus), (**A**) and DFT pore size distribution (silica, ads. branch model, cylindrical pores) of ZEO X (rhombus), (**B**).

Table 2. SSA_{BET} and pore volume of kaolinite, ZEO A and ZEO X.

	SSA_{BET} [$m^2 \cdot g^{-1}$]	Pore Volume [$cc \cdot Å^{-1} \cdot g^{-1}$]	
		V micro [<20 Å]	V meso [20–500 Å]
Kaolinite	9	/	0.035
ZEO A	11	/	0.035
ZEO X	460	0.19	0.05

The N_2 physisorption isotherm of kaolinite (Figure 5A) is characterized as a type III isotherm, typical of a non-porous material [57]. In this case, the host–guest interactions between the surface of the parent clay and the N_2 molecules are relatively weak, and the absence of hysteresis is consistent with the almost complete lack of mesopores [57,58]. The negligible gas uptake between 0 and ca. 0.7 P/P_0 suggests that the N_2 molecules are clustered at the adsorption sites located on the surface of the particles and in the macropores arising from the aggregation of the clusters of lamellae [57,58]. The SSA_{BET} of the parent kaolinite corresponds to 9 $m^2 \cdot g^{-1}$, whereas its cumulative pore volume is 0.035 $cc \cdot g^{-1}$.

The N_2 physisorption isotherm of ZEO A appears quite similar to that of kaolinite. Again, the isotherm reflects a type III isotherm, free of a hysteresis loop and typically found for non-porous materials [57,58]. This result was already observed in the literature; the Na^+ extra-framework cations located in four-ring sites, near the entrances of the supercages (Site III, see Figure S2A), hinder the diffusion of the N_2 molecules within the micropores [39,40,59]. Hence, no gas uptake is observed between 0 and 0.8 P/P_0, and the adsorbate molecules occupy the external surfaces of the sample and the macropores due to the crystal's aggregation [57,58]. Despite several other evidence (i.e., XRPD and MAS NMR) suggesting that the sample has an evident LTA microporous structure, N_2 physisorption analysis at 77 K could not provide a correct estimation of the SSA_{BET} and the pore volume of ZEO, with results that are much lower than the real ones and correspond to 11 $m^2 \cdot g^{-1}$ and 0.035 $cc \cdot g^{-1}$.

The N_2 physisorption isotherm of ZEO X is reported in Figure 5. Despite the first section of the curve reflecting a type I model, the presence of an H4 hysteresis loop suggests that the curve could be more compatible with a type IV(a) isotherm [57,58]. The H_4 hysteresis loop is often found in the adsorption isotherms of zeolites due to aggregated crystals [57,58], and the steep N_2 uptake at low relative gas pressures is attributed to

enhanced host–guest interactions that occur in narrow micropores [57,58]. In fact, as it can be derived from the results of the DFT analysis (Figure 5B), ZEO X is characterized by a narrow pore size distribution centered at 7 Å. As reported in the literature, the pore size distribution of zeolites X in the Na^+ form should be approximately 10 Å [60]. This difference is due to the fact that in our case N_2 was used, whereas the literature result was obtained from an Ar adsorption isotherm [60]. No other peaks were observed, thus suggesting that the main contribution to the pore volume of the sample mainly comes from the micropores, which show a micropore volume of 0.19 $cc \cdot g^{-1}$, whereas those of meso- and macropore are only 0.05 $cc \cdot g^{-1}$. The SSA_{BET} of ZEO X has been assessed at 460 $m^2 \cdot g^{-1}$.

The excess adsorption of CO_2 in the different zeolites was assessed by means of a custom-built volumetric apparatus (for more details about the building scheme and the experimental steps see Supporting Information). The CO_2 excess adsorption isotherms up to ca. 1 bar of gas pressure and 298 K are shown in Figure 6.

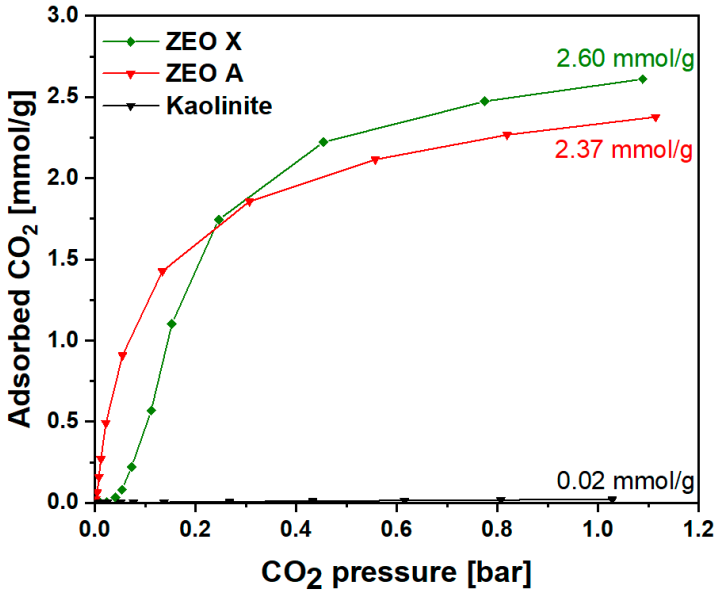

Figure 6. CO_2 adsorption isotherms at about 1 bar of gas pressure and 25 °C on kaolinite (triangles), ZEO A (squares) and ZEO X (rhombus). Prior to the analyses, the sample were treated at 180 °C for 17 h under vacuum (residual pressure < 10^{-3} mbar).

Kaolinite has a reduced CO_2 uptake, equal to 0.02 mmol/g, which is due to its low SSA_{BET} and pore volume. However, ZEO A, which has similar SSA and pore volume compared to the parent kaolinite, shows a much larger CO_2 adsorption capacity of ca. 2.37 mmol of CO_2 per gram of material at 25 °C and ca. 1 bar of gas pressure. The highest adsorption capacity is reached by ZEO X with a CO_2 uptake of 2.60 mmol/g. The results are in agreement with those found in the literature [16,32]. Moreover, as reported in Figure S3, the CO_2 adsorption measurement on ZEO X has been repeated upon thermally treating the same sample at 160 °C for 12 h under vacuum resulting in the same adsorption capacity. Thanks to the presence of a high microporous volume and narrow micropores of 7 Å (Figure 5B, Table 2), the CO_2 adsorption isotherm of ZEO X shows a steep CO_2 uptake between 0 and 0.3 bar. In fact, at low gas pressures and ambient temperature, micropores represent the most energetic and favorable adsorption sites for CO_2 molecules [61,62]. A similar trend can be observed for ZEO A. However, the CO_2 adsorption capacity of ZEO A below 0.2 bar is higher than that of ZEO X. This behavior might be related to the different pore sizes of ZEO A and ZEO X. In fact, as reported in the literature, zeolites A with Na^+ extra-framework cations are characterized by an 8-ring supercage of ca. 4 Å [63]. As reported in the literature, at low gas pressure, the density of the CO_2 molecules is highest in smaller pores, while at higher gas pressures larger pores show a higher adsorptive capability [61,62]. Thereby, the higher CO_2 adsorption capacity of ZEO A below 0.2 bar

can be explained, as ZEO X is characterized by micropores of 7 Å, whereas, based on the literature [63], it is reasonable to assume that the micropore width of ZEO A should have micropores of ca. 4 Å. As it has already been reported in the literature [14], the observed high affinity between the adsorbent and the adsorbate can be explained by considering that the permanent quadrupole moment of the CO_2 molecule can give rise to non-covalent electrostatic interactions with Na^+ cations [14,15]. An additional effect acting on the electropositive C atom of the CO_2 molecule is its interaction with the BrØnsted oxygen (Al-O^--Si) through an acid–base mechanism [14,15].

4. Conclusions

In this work, natural kaolinite was used as a more cost-effective and widely available source of Si and Al for the synthesis of a zeolite A (ZEO A) and a zeolite X (ZEO X) under mild conditions. ZEO A was obtained through the alkaline fusion of the parent clay in the presence of NaOH as an alkali activator, whereas a high-purity zeolite X, coded as ZEO X, was synthesized upon the addition of sodium metasilicate to the mixture along with kaolinite and NaOH to obtain the favorable SiO_2/Al_2O_3 molar ratio for zeolites X.

The results of the XRPD measurements and the ^{29}Si and ^{27}Al MAS NMR measurements show that ZEO A contains traces of a zeolite X phase, which represents ca. the 1 wt.% that was probably formed due to the partial mineralization of some Si-rich impurities within the parent kaolinite (such as quartz, illite and montmorillonite), which would have slightly increased the Si content of the preliminary mixture. The results of the Rietveld semiquantitative analysis revealed that almost all the kaolinite phases within the parent clay have been successfully converted into the zeolite A phase. On the other hand, the XRPD pattern of ZEO X is dominated only by the reflections of a zeolite X, and based on the Rietveld semiquantitative analysis and the detected crystalline phases, it was determined that the zeolite X phase approached 100 wt.%. However, the results of the ^{27}Al MAS NMR measurement revealed the presence of some residues or by-products with amorphous structures, containing octahedrally coordinated Al.

Both the morphological characterization using SEM and the elemental analysis using EDX showed clearly the conversion of the layered clay to cubic-shaped microcrystals and the incorporation of Na^+ to compensate for the charge effects from the Si/Al variance. The textural properties of the different materials were investigated through N_2 physisorption analysis. Kaolinite is characterized by a low SSA_{BET}, equal to 9 $m^2 \cdot g^{-1}$ and a pore volume limited to intercrystalline mesoporosity. A similar result, with an apparent absence of microporosity, was observed for ZEO A, as, according to the literature, the Na^+ extra-framework cations lying at the entrances of the supercage hinder the diffusion of N_2 molecules into the cavities of the sample. On the other hand, due to the different structure, ZEO X shows a SSA_{BET} of 460 $m^2 \cdot g^{-1}$, a microporous volume of 0.19 $cc \cdot g^{-1}$ and a total pore volume of 0.24 $cc \cdot g^{-1}$.

To evaluate a possible application in the field of carbon capture and storage, CO_2 adsorption at 25 °C and up to 1 bar was assessed for all the synthesized materials. The excess adsorption of the parent kaolinite, ZEO A and ZEO X was investigated by means of a prototype volumetric apparatus. Kaolinite shows a very limited CO_2 adsorption capacity, while the CO_2 adsorption capacity of ZEO A and ZEO X were found to be 2.60 and 2.37 mmol/g, respectively, at ca. 1 bar of gas pressure and 25 °C. Moreover, it was demonstrated that the ZEO X sample can be thermally regenerated without any significant loss of its CO_2 adsorption capacity.

Supplementary Materials: The following supporting information can be downloaded at: https://www.mdpi.com/article/10.3390/pr12010194/s1, Table S1: Rietveld semiquantitative analysis of the parent kaolinite (no external standard for amorphous phase determination was used); Table S2: Rietveld semiquantitative analysis of ZEO A and ZEO X (no external standard for amorphous phase determination was used); Figure S1: Sites that can be populated by extra-framework cations within a zeolite A, (a), and a zeolite X, (b), adapted from [14,54]; Figure S2: Snapshot, (A), and building scheme, (B), of the custom-built volumetric apparatus; Figure S3: CO_2 adsorption isotherms at 25 °C

of a commercial carbon performed on the volumetric apparatus (rhombus) and on the automatic system; Figure S4: CO_2 adsorption isotherm on ZEO X at 25 °C and up to ca. 1 bar of gas pressure (rhombus). The same sample was thermally treated at 160 °C for 12 h under vacuum and the adsorption measurement was repeated following the same procedure (triangles). (see Ref. [64])

Author Contributions: Conceptualization, G.C., E.B. and C.B.; methodology, G.C., F.B. and G.P.; validation, G.C. and F.B.; investigation, G.C., F.B., L.M. and G.P.; resources, C.B., L.M. and E.B.; data curation, G.C., F.B. and G.P.; writing—original draft preparation, G.C., G.P. and F.B.; writing—review and editing, C.B., V.M. and E.B.; supervision, C.B. and E.B.; project administration, C.B.; funding acquisition, C.B., L.M. and E.B. All authors have read and agreed to the published version of the manuscript.

Funding: This research was funded by the SATURNO project "Organic waste and carbon dioxide transformed into fuels, fertilizers and chemicals; concrete application of circular economy" (FESR 2014/2020) technological platform (Bioeconomy I.1b.2.2_14/20_Bioeconomics—Project code 333-19), Piedmont region (2019–2022). E.B. acknowledges the Università del Piemonte Orientale founding scheme "Fondi di Ateneo per la Ricerca anno 2017" for the economic support of the project "Processi sostenibili finalizzati alla valorizzazione di materiali e materiali naturali per usi funzionali".

Data Availability Statement: Data are contained within the article and Supplementary Materials.

Conflicts of Interest: The authors declare no conflicts of interest.

References

1. Yaacob, N.F.F.; Mat Yazid, M.R.; Abdul Maulud, K.N.; Ahmad Basri, N.E. A Review of the Measurement Method, Analysis and Implementation Policy of Carbon Dioxide Emission from Transportation. *Sustainability* **2020**, *12*, 5873. [CrossRef]
2. Li, Q.; Han, Y.; Liu, X.; Ansari, U.; Cheng, Y.; Yan, C. Hydrate as a By-Product in CO_2 Leakage during the Long-Term Sub-Seabed Sequestration and Its Role in Preventing Further Leakage. *Environ. Sci. Pollut. Res.* **2022**, *29*, 77737–77754. [CrossRef] [PubMed]
3. Kweku, D.; Bismark, O.; Maxwell, A.; Desmond, K.; Danso, K.; Oti-Mensah, E.; Quachie, A.; Adormaa, B. Greenhouse Effect: Greenhouse Gases and Their Impact on Global Warming. *J. Sci. Res. Rep.* **2018**, *17*, 1–9. [CrossRef]
4. Madejski, P.; Chmiel, K.; Subramanian, N.; Kuś, T. Methods and Techniques for CO_2 Capture: Review of Potential Solutions and Applications in Modern Energy Technologies. *Energies* **2022**, *15*, 887. [CrossRef]
5. Ochedi, F.O.; Liu, Y.; Adewuyi, Y.G. State-of-the-Art Review on Capture of CO_2 Using Adsorbents Prepared from Waste Materials. *Process Saf. Environ. Prot.* **2020**, *139*, 1–25. [CrossRef]
6. Varvoutis, G.; Lampropoulos, A.; Mandela, E.; Konsolakis, M.; Marnellos, G. Recent Advances on CO_2 Mitigation Technologies: On the Role of Hydrogenation Route via Green H_2. *Energies* **2022**, *15*, 4790. [CrossRef]
7. Woodall, C.M.; Fan, Z.; Lou, Y.; Bhardwaj, A.; Khatri, A.; Agrawal, M.; McCormick, C.F.; Friedmann, S.J. Technology Options and Policy Design to Facilitate Decarbonization of Chemical Manufacturing. *Joule* **2022**, *6*, 2474–2499. [CrossRef]
8. Vinoba, M.; Bhagiyalakshmi, M.; Alqaheem, Y.; Alomair, A.A.; Pérez, A.; Rana, M.S. Recent Progress of Fillers in Mixed Matrix Membranes for CO_2 Separation: A Review. *Sep. Purif. Technol.* **2017**, *188*, 431–450. [CrossRef]
9. Park, Y.; Ju, Y.; Park, D.; Lee, C.-H. Adsorption Equilibria and Kinetics of Six Pure Gases on Pelletized Zeolite 13X up to 1.0 MPa: CO_2, CO, N_2, CH_4, Ar and H_2. *Chem. Eng. J.* **2016**, *292*, 348–365. [CrossRef]
10. Dean, C.C.; Blamey, J.; Florin, N.H.; Al-Jeboori, M.J.; Fennell, P.S. The Calcium Looping Cycle for CO_2 Capture from Power Generation, Cement Manufacture and Hydrogen Production. *Chem. Eng. Res. Des.* **2011**, *89*, 836–855. [CrossRef]
11. Celoria, G.; Miglio, V.; Paul, G.; Bisio, C.; Golemme, G.; Boccaleri, E. Silica Particles Derived from Natural Kaolinite for the Removal of Rhodamine B from Polluted Water. *Processes* **2022**, *10*, 964. [CrossRef]
12. Miglio, V.; Zaccone, C.; Vittoni, C.; Braschi, I.; Buscaroli, E.; Golemme, G.; Marchese, L.; Bisio, C. Silica Monolith for the Removal of Pollutants from Gas and Aqueous Phases. *Molecules* **2021**, *26*, 1316. [CrossRef] [PubMed]
13. Paul, G.; Begni, F.; Melicchio, A.; Golemme, G.; Bisio, C.; Marchi, D.; Cossi, M.; Marchese, L.; Gatti, G. Hyper-Cross-Linked Polymers for the Capture of Aromatic Volatile Compounds. *ACS Appl. Polym. Mater.* **2020**, *2*, 647–658. [CrossRef]
14. Walton, K.S.; Abney, M.B.; Douglas LeVan, M. CO_2 Adsorption in Y and X Zeolites Modified by Alkali Metal Cation Exchange. *Microporous Mesoporous Mater.* **2006**, *91*, 78–84. [CrossRef]
15. Bonenfant, D.; Kharoune, M.; Niquette, P.; Mimeault, M.; Hausler, R. Advances in Principal Factors Influencing Carbon Dioxide Adsorption on Zeolites. *Sci. Technol. Adv. Mater.* **2008**, *9*, 013007. [CrossRef]
16. Garshasbi, V.; Jahangiri, M.; Anbia, M. Equilibrium CO_2 Adsorption on Zeolite 13X Prepared from Natural Clays. *Appl. Surf. Sci.* **2017**, *393*, 225–233. [CrossRef]
17. Kerstens, D.; Smeyers, B.; Van Waeyenberg, J.; Zhang, Q.; Yu, J.; Sels, B.F. State of the Art and Perspectives of Hierarchical Zeolites: Practical Overview of Synthesis Methods and Use in Catalysis. *Adv. Mater.* **2020**, *32*, 2004690. [CrossRef]
18. Cundy, C.S.; Cox, P.A. The Hydrothermal Synthesis of Zeolites: History and Development from the Earliest Days to the Present Time. *Chem. Rev.* **2003**, *103*, 663–702. [CrossRef]

19. Salehi, S.; Anbia, M. Characterization of CPs/Ca-Exchanged FAU- and LTA-Type Zeolite Nanocomposites and Their Selectivity for CO_2 and N_2 Adsorption. *J. Phys. Chem. Solids* **2017**, *110*, 116–128. [CrossRef]
20. Szostak, R. *Molecular Sieves: Principles of Synthesis and Identification*; Springer: Dordrecht, The Netherlands, 1989; ISBN 978-94-010-9531-0.
21. Khaleque, A.; Alam, M.M.; Hoque, M.; Mondal, S.; Haider, J.B.; Xu, B.; Johir, M.A.H.; Karmakar, A.K.; Zhou, J.L.; Ahmed, M.B.; et al. Zeolite Synthesis from Low-Cost Materials and Environmental Applications: A Review. *Environ. Adv.* **2020**, *2*, 100019. [CrossRef]
22. Baerlocher, C.; Meier, W.M.; Olson, D.H.; Meier, W.M. (Eds.) *Atlas of Zeolite Framework Types*, 5th ed.; Elsevier: Amsterdam, The Netherlands; New York, NY, USA, 2001; ISBN 978-0-444-50701-3.
23. Alaba, P.A.; Sani, Y.M.; Ashri Wan Daud, W.M. Kaolinite Properties and Advances for Solid Acid and Basic Catalyst Synthesis. *RSC Adv.* **2015**, *5*, 101127–101147. [CrossRef]
24. Bhattacharyya, K.G.; Gupta, S.S. Adsorption of a Few Heavy Metals on Natural and Modified Kaolinite and Montmorillonite: A Review. *Adv. Colloid. Interface Sci.* **2008**, *140*, 114–131. [CrossRef]
25. Wang, S.; Gainey, L.; Mackinnon, I.D.R.; Xi, Y. High- and Low-Defect Kaolinite for Brick Making: Comparisons of Technological Properties, Phase Evolution and Microstructure. *Constr. Build. Mater.* **2023**, *366*, 130250. [CrossRef]
26. Burst, J.F. The Application of Clay Minerals in Ceramics. *Appl. Clay Sci.* **1991**, *5*, 421–443. [CrossRef]
27. Glid, M.; Sobrados, I.; Rhaiem, H.B.; Sanz, J.; Amara, A.B.H. Alkaline Activation of Metakaolinite-Silica Mixtures: Role of Dissolved Silica Concentration on the Formation of Geopolymers. *Ceram. Int.* **2017**, *43*, 12641–12650. [CrossRef]
28. Ma, Y.; Yan, C.; Alshameri, A.; Qiu, X.; Zhou, C.; Li, D. Synthesis and Characterization of 13X Zeolite from Low-Grade Natural Kaolin. *Adv. Powder Technol.* **2014**, *25*, 495–499. [CrossRef]
29. Abdullahi, T.; Harun, Z.; Othman, M.H.D. A Review on Sustainable Synthesis of Zeolite from Kaolinite Resources via Hydrothermal Process. *Adv. Powder Technol.* **2017**, *28*, 1827–1840. [CrossRef]
30. Belviso, C.; Cavalcante, F.; Niceforo, G.; Lettino, A. Sodalite, Faujasite and A-Type Zeolite from 2:1dioctahedral and 2:1:1 Trioctahedral Clay Minerals. A Singular Review of Synthesis Methods through Laboratory Trials at a Low Incubation Temperature. *Powder Technol.* **2017**, *320*, 483–497. [CrossRef]
31. Ayele, L.; Pérez-Pariente, J.; Chebude, Y.; Díaz, I. Conventional versus Alkali Fusion Synthesis of Zeolite A from Low Grade Kaolin. *Appl. Clay Sci.* **2016**, *132–133*, 485–490. [CrossRef]
32. Lee, J.-S.; Kim, J.-H.; Kim, J.-T.; Suh, J.-K.; Lee, J.-M.; Lee, C.-H. Adsorption Equilibria of CO_2 on Zeolite 13X and Zeolite X/Activated Carbon Composite. *J. Chem. Eng. Data* **2002**, *47*, 1237–1242. [CrossRef]
33. Li, J.; Gao, M.; Yan, W.; Yu, J. Regulation of the Si/Al Ratios and Al Distributions of Zeolites and Their Impact on Properties. *Chem. Sci.* **2023**, *14*, 1935–1959. [CrossRef] [PubMed]
34. Khalifa, A.Z.; Cizer, Ö.; Pontikes, Y.; Heath, A.; Patureau, P.; Bernal, S.A.; Marsh, A.T.M. Advances in Alkali-Activation of Clay Minerals. *Cem. Concr. Res.* **2020**, *132*, 106050. [CrossRef]
35. Daou, I.; Lecomte-Nana, G.; Tessier-Doyen, N.; Peyratout, C.; Gonon, M.; Guinebretiere, R. Probing the Dehydroxylation of Kaolinite and Halloysite by In Situ High Temperature X-ray Diffraction. *Minerals* **2020**, *10*, 480. [CrossRef]
36. Salahudeen, N.; Ahmed, A.S.; Al-Muhtaseb, A.H.; Dauda, M.; Waziri, S.M.; Jibril, B.Y. Synthesis and Characterization of Micro-Sized Silica from Kankara Kaolin. *J. Eng. Res.* **2014**, *19*, 27–32.
37. Temuujin, J.; Burmaa, G.; Amgalan, J.; Okada, K. Preparation of Porous Silica from Mechanically Activated Kaolinite. *J. Porous Mater.* **2001**, *8*, 233–238. [CrossRef]
38. Marsh, A.; Heath, A.; Patureau, P.; Evernden, M.; Walker, P. Alkali Activation Behaviour of Un-Calcined Montmorillonite and Illite Clay Minerals. *Appl. Clay Sci.* **2018**, *166*, 250–261. [CrossRef]
39. Pillai, R.S.; Sebastian, J.; Jasra, R.V. Grand Canonical Monte Carlo Simulation and Volumetric Equilibrium Studies for Adsorption of Nitrogen, Oxygen, and Argon in Cadmium (II) Exchanged Zeolite A. *J. Porous Mater.* **2012**, *19*, 683–693. [CrossRef]
40. Tahraoui, Z.; Nouali, H.; Marichal, C.; Forler, P.; Klein, J.; Daou, T.J. Influence of the Compensating Cation Nature on the Water Adsorption Properties of Zeolites. *Molecules* **2020**, *25*, 944. [CrossRef]
41. Fernandez, R.; Martirena, F.; Scrivener, K.L. The Origin of the Pozzolanic Activity of Calcined Clay Minerals: A Comparison between Kaolinite, Illite and Montmorillonite. *Cem. Concr. Res.* **2011**, *41*, 113–122. [CrossRef]
42. Paul, G.; Bisio, C.; Braschi, I.; Cossi, M.; Gatti, G.; Gianotti, E.; Marchese, L. Combined Solid-State NMR, FT-IR and Computational Studies on Layered and Porous Materials. *Chem. Soc. Rev.* **2018**, *47*, 5684–5739. [CrossRef]
43. Marsh, A.; Heath, A.; Patureau, P.; Evernden, M.; Walker, P. A Mild Conditions Synthesis Route to Produce Hydrosodalite from Kaolinite, Compatible with Extrusion Processing. *Microporous Mesoporous Mater.* **2018**, *264*, 125–132. [CrossRef]
44. Hayashi, S.; Ueda, T.; Hayamizu, K.; Akiba, E. NMR Study of Kaolinite. 1. Silicon-29, Aluminum-27, and Proton Spectra. *J. Phys. Chem.* **1992**, *96*, 10922–10928. [CrossRef]
45. Moran, K.L.; Dupree, R.; Barker, P.D.; Readman, J.E.; Edwards, P.P.; Anderson, P.A. ^{29}Si and ^{27}Al MAS NMR Spectra Are Affected by Alkali Metal Cluster Formation in Zeolite LTA. *Chem. Commun.* **2000**, 55–56. [CrossRef]
46. Dyballa, M.; Obenaus, U.; Lang, S.; Gehring, B.; Traa, Y.; Koller, H.; Hunger, M. Brønsted Sites and Structural Stabilization Effect of Acidic Low-Silica Zeolite A Prepared by Partial Ammonium Exchange. *Microporous Mesoporous Mater.* **2015**, *212*, 110–116. [CrossRef]

47. Poumaye, N.; Allahdin, O.; Tricot, G.; Revel, B.; Billon, G.; Recourt, P.; Wartel, M.; Boughriet, A. MAS NMR Investigations on a Metakaolinite-Rich Brick after Zeolitization by Alkaline Treatments. *Microporous Mesoporous Mater.* **2019**, *277*, 1–9. [CrossRef]
48. Madani, A.; Aznar, A.; Sanz, J.; Serratosa, J.M. Silicon-29 and Aluminum-27 NMR Study of Zeolite Formation from Alkali-Leached Kaolinites: Influence of Thermal Preactivation. *J. Phys. Chem.* **1990**, *94*, 760–765. [CrossRef]
49. Clayden, N.; Esposito, S.; Ferone, C.; Michele, P. ^{29}SI and ^{27}Al NMR Study of the Thermal Transformation of Barium Exchanged Zeolite-A to Celsian. *J. Mater. Chem.* **2003**, *13*, 1681–1685. [CrossRef]
50. Grass, J.-P.; Klühspies, K.; Reiprich, B.; Schwieger, W.; Inayat, A. Layer-Like Zeolite X as Catalyst in a Knoevenagel Condensation: The Effect of Different Preparation Pathways and Cation Exchange. *Catalysts* **2021**, *11*, 474. [CrossRef]
51. Greiser, S.; Hunger, M.; Jäger, C. 29Si{27Al} TRAPDOR MAS NMR to Distinguish Q (mAl) Sites in Aluminosilicates. Test Case: Faujasite-Type Zeolites. *Solid. State Nucl. Magn. Reson.* **2016**, *79*, 6–10. [CrossRef]
52. Zhang, Q.; Yan, Z.; Ouyang, J.; Zhang, Y.; Yang, H.; Chen, D. Chemically Modified Kaolinite Nanolayers for the Removal of Organic Pollutants. *Appl. Clay Sci.* **2018**, *157*, 283–290. [CrossRef]
53. Seidel, A.; Schimiczek, B.; Tracht, U.; Boddenberg, B. 23Na Solid State MAS NMR of Sodium Halides Occluded in Zeolites. *Solid. State Nucl. Magn. Reson.* **1997**, *9*, 129–141. [CrossRef] [PubMed]
54. Kaushik, V.K.; Vijayalakshmi, R.P.; Choudary, N.V.; Bhat, S.G.T. XPS Studies on Cation Exchanged Zeolite Aq. *Microporous Mesoporous Mater.* **2002**, *51*, 139–144. [CrossRef]
55. De Peña, Y.P.; Rondón, W. Linde Type a Zeolite and Type Y Faujasite as a Solid-Phase for Lead, Cadmium, Nickel and Cobalt Preconcentration and Determination Using a Flow Injection System Coupled to Flame Atomic Absorption Spectrometry. *Am. J. Anal. Chem.* **2013**, *4*, 387–397. [CrossRef]
56. Awad, A.M.; Shaikh, S.M.R.; Jalab, R.; Gulied, M.H.; Nasser, M.S.; Benamor, A.; Adham, S. Adsorption of Organic Pollutants by Natural and Modified Clays: A Comprehensive Review. *Sep. Purif. Technol.* **2019**, *228*, 115719. [CrossRef]
57. Thommes, M.; Kaneko, K.; Neimark, A.V.; Olivier, J.P.; Rodriguez-Reinoso, F.; Rouquerol, J.; Sing, K.S.W. Physisorption of Gases, with Special Reference to the Evaluation of Surface Area and Pore Size Distribution (IUPAC Technical Report). *Pure Appl. Chem.* **2015**, *87*, 1051–1069. [CrossRef]
58. Rouquerol, F.; Rouquerol, J.; Sing, K.S.W. *Adsorption by Powders and Porous Solids: Principles, Methodology, and Applications*; Academic Press: San Diego, CA, USA, 1999; ISBN 978-0-12-598920-6.
59. Shang, Y.; Wu, J.; Zhu, J.; Wang, Y.; Meng, C. Study on Adsorption of N_2 and O_2 by Magnesium (II)-Exchanged Zeolite A. *J. Alloys Compd.* **2009**, *478*, L5–L7. [CrossRef]
60. Lee, S.; Kim, H.; Choi, M. Controlled Decationization of X Zeolite: Mesopore Generation within Zeolite Crystallites for Bulky Molecular Adsorption and Transformation. *J. Mater. Chem. A* **2013**, *1*, 12096–12102. [CrossRef]
61. Presser, V.; McDonough, J.; Yeon, S.-H.; Gogotsi, Y. Effect of Pore Size on Carbon Dioxide Sorption by Carbide Derived Carbon. *Energy Environ. Sci.* **2011**, *4*, 3059. [CrossRef]
62. Samios, S.; Stubos, A.K.; Kanellopoulos, N.K.; Cracknell, R.F.; Papadopoulos, G.K.; Nicholson, D. Determination of Micropore Size Distribution from Grand Canonical Monte Carlo Simulations and Experimental CO_2 Isotherm Data. *Langmuir* **1997**, *13*, 2795–2802. [CrossRef]
63. Canosa, E.; Norrehed, S. Adsorbents for Pollution Reduction in Cultural Heritage Collections. *Riksantikvarieämbetet* **2019**. [CrossRef]
64. Lowell, S.; Shields, J.E.; Thomas, M.A.; Thommes, M. *Characterization of Porous Solids and Powders: Surface Area, Pore Size and Density*; Particle Technology Series; Springer: Dordrecht, The Netherlands, 2004; Volume 16, Chapter 14; ISBN 978-90-481-6633-6.